# Acoustic Loss of GHz Higher-Order Lamb Waves in Thin-Film Lithium Niobate: A Comparative Study

Ruochen Lu, *Member, IEEE*, Yansong Yang, *Member, IEEE*, and Songbin Gong, *Senior Member, IEEE*

*Abstract*—**This work reports a comparative study of acoustic loss between different Lamb waves at GHz in thin-film lithium niobate (LiNbO₃). The propagation loss (PL) of higher-order Lamb waves in thin-film LiNbO₃ is studied for the first time using acoustic delay line (ADL) testbeds. The acoustic wave attenuation and quality factors ($Q$) of different Lamb waves are extracted, showing higher $Q$s for higher-order Lamb modes than fundamental modes in air and vacuum at room temperature. The extracted $Q$s are higher than those reported in thin-film LiNbO₃ resonators, implying the electrode and anchor-induced loss as the dominant loss factors. The ADL-based loss analysis framework is readily extendable to acoustic damping study in other microwave acoustic platforms.**     **[2021-0165]**

*Index Terms*—**Acoustic attenuation, acoustic delay line, lithium niobate, quality factor, thin-film devices, Lamb mode.**

## I. INTRODUCTION

**A**COUSTIC devices operating beyond GHz have been extensively studied in the past few years [1], [2]. The development is fueled by the endeavor to scale acoustic signal processing elements (e.g., piezoelectric resonator-based filters) into 5G frequency bands [3]. Acoustic devices could offer smaller footprints and better frequency selectivity than their electromagnetic (EM) counterparts, suitable for mobile applications [4]. Conventionally, the frequency scaling is achieved by reducing critical dimensions, such as the electrode pitch width in surface acoustic wave (SAW) devices [5] and the stack thickness in film bulk acoustic resonators (FBAR) [6]. However, further dimension reduction is challenging, as acoustic wavelengths fall into the sub-micron regime, causing microfabrication challenges and increasing acoustic and EM loss [7]–[9]. Higher frequency acoustic devices call for novel designs.

One promising frequency scaling scheme is using higher-order modes in piezoelectric thin films, e.g., lithium niobate (LiNbO₃) [10]–[15] and aluminum/scandium aluminum nitride (AlN/ScAlN) [16]–[23]. Different from fundamental modes, e.g., fundamental symmetric (S0) [24]–[27]

and shear horizontal (SH0) [28]–[31] modes, higher-order Lamb modes have displacement nodes in the thickness direction, e.g., first-order antisymmetric (A1) [10], [32] first-order symmetrical (S1) [11], [33], and even higher-order Lamb modes [34], [35]. The operating frequencies of such modes are collectively determined by lateral and thickness dimensions [36], higher than fundamental modes in the same film stack with the same lateral wavelength. However, the loss of higher-order Lamb waves remains largely unstudied. Conventionally, $Q$ studies in suspended microelectromechanical systems (MEMS) devices analyze the maximum achievable quality factor ($Q$) in resonators [37]–[39]. However, a similar process is especially difficult for GHz higher-order Lamb modes, as pronounced acoustic/EM loss in electrodes is hard to isolate and measure their contributions individually.

Recently, the authors report an experimental study on acoustic attenuation of S0 and SH0 in thin-film LiNbO₃ using acoustic delay lines (ADLs) [9], validating intrinsically low damping in the transferred thin-film. However, such a study is not directly applicable to higher-order Lamb waves. First, higher-order Lamb waves tend to be confined between electrodes and hard to propagate unless explicitly designed [40]. Second, higher-order modes are highly dispersive [36] and show different group ($v_g$) and phase velocities ($v_p$). The relation between propagation loss (PL) and $Q$ in higher-order Lamb modes is not reported. A universal framework is highly sought after.

This work presents a comparative study of acoustic loss between GHz Lamb waves with different mode orders in thin-film LiNbO₃. ADLs with identical transducers but different gap lengths are studied as testbeds, using a generalized approach for $Q$ extraction. The results show higher acoustic $Q$s of A1 and second-order symmetrical (S2) than S0 and SH0 in air and vacuum at room temperature, validating the prior frequency scaling scheme. The extracted $Q$s are higher than those reported in resonators, implying improvement opportunities in topology design and electrode optimization. The approach is readily extendable to other emerging acoustic platforms.

## II. DESIGN AND SIMULATION

### A. Acoustic Delay Line Testbed

The ADL testbed follows the structure reported in [40] (Fig. 1). A pair of 100 nm thick aluminum (Al) interdigitated transducers are placed on the opposite end of the suspended 1600 nm Z-cut LiNbO₃. Unlike the prior study on PL of S0 and SH0 [9], bi-directional transducers are

TABLE I
DESIGN PARAMETERS OF ADL TESTBEDS

| Sym. | Parameter | Value | Sym. | Parameter | Value |
|------|-----------|-------|------|-----------|-------|
| $\Lambda$ | Cell length (µm) | 3.5-6.5 | $W_a$ | Aperture width (µm) | 100 |
| $N$ | Number of cells | 4 | $L_g$ | Gap length (µm) | 10-800 |
| $T_{LN}$ | LiNbO$_3$ thickness (nm) | 1600 | $T_{Al}$ | Electrode thickness (nm) | 100 |
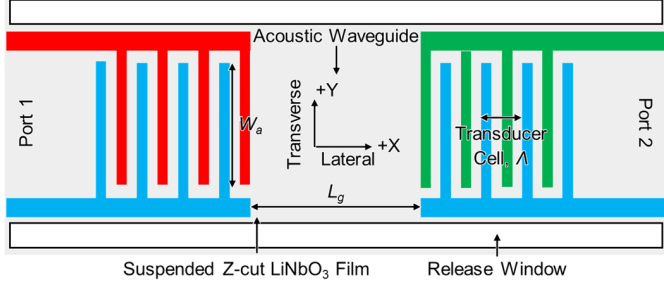


Fig. 1. Mockup of an ADL testbed on a suspended Z-cut LiNbO3 thin film.
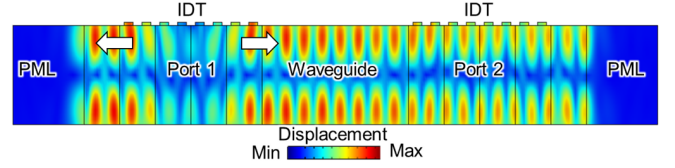


Fig. 2. Displacement mode shape of ADL in A1 passband. The thickness dimension is scaled.



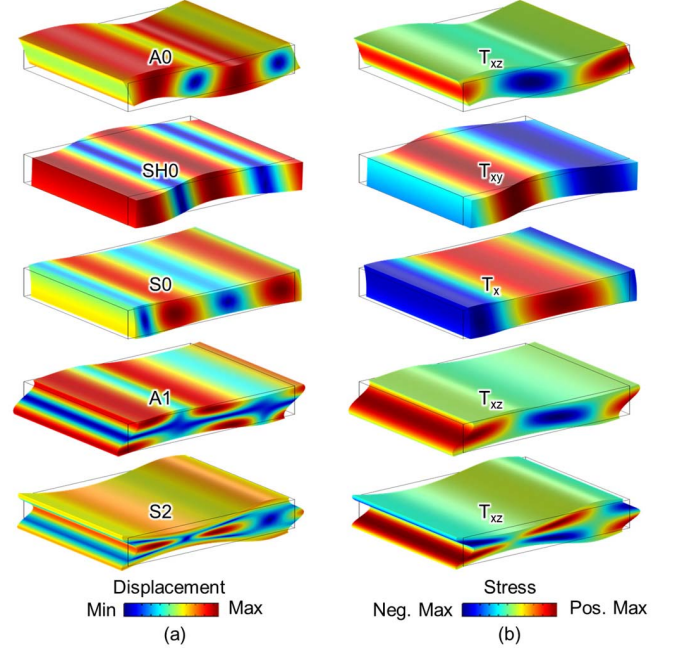Fig. 3. Mode shapes of Lamb modes with different mode orders in both (a) displacement and (b) dominant stress formats.

implemented due to the limited bandwidth of higher-order Lamb mode unidirectional transducers [41]. To mitigate the intrinsic triple-echo in bi-directional ADLs, 4 unit cells are used to create the impedance mismatch, thus significantly attenuating the echos [42].

Z-cut LiNbO$_3$ is used in this work, as different Lamb modes can be excited with the transducers. More specifically, ADLs with the lateral side placed along the material X-axis excite fundamental antisymmetric (A0), SH0, A1, and S2, while those placed along the material Y-axis excite A0 and S0 A1, and S2 [40]. The mode shapes are plotted in Fig. 2. The input EM signals in the passband of a certain passband are converted into the corresponding acoustic vibrations, propagate toward the output ports before being converted back into the EM domain (Fig. 2).

PL and $v_g$ of different modes are measured and analyzed from the insertion loss (IL) and group delay of ADLs with different gap lengths ($L_g$). PL is studied with a port extension approach [43], and the transducer effects are mitigated by extracting the slope of IL over $L_g$. Similarly, $v_g$ is obtained from the slope of group delay over $L_g$. The acoustic $Q$s of these highly dispersive modes are calculated with PL and $v_g$, which will be explained in Section II-C. Wideband results are studied by implementing ADL groups with different cell lengths ($\Lambda$). In this work, we implement testbeds with $\Lambda$ between 3.5 and 6.5 $\mu$m. The range of lateral wavelengths between 3.5 and 6.5 $\mu$m is used here to match the designed transducer, and thus far from the cut-off of A1 and S2 in 1.6 $\mu$m thick LiNbO$_3$ to generate propagating waves [40]. $L_g$ between 10 and 800 $\mu$m are used here, as longer ADLs are preferred for more accurate extraction but suffer from lower fabrication yield. A fixed aperture width ($W_a$) of 100 $\mu$m is used as it is significantly larger than $\Lambda$ to maintain plane wave properties while allowing the release of ADLs on the same die with isotropic dry etch simultaneously.

### B. Higher-Order Lamb Waves in Z-Cut LiNbO$_3$

The dispersion of Lamb waves is first studied with COMSOL finite element analysis (FEA). Unit cells with a lateral length of $\Lambda$ in 1600 nm thick Z-cut LiNbO$_3$ thin films are simulated in eigenmode FEA. EM and acoustic periodic boundary conditions are applied in the vertical surfaces. Mechanically free condition is applied to the top and bottom. Electrically open is used for the bottom. Electrically open and short are applied to the top to obtain $f_{p\_open}$ and $f_{p\_short}$ at different $\Lambda$, respectively. The key parameters of $v_p$, $v_g$, and $K^2$ are calculated as [40], [44]:

$$v_{p\_open} = f_{open} \cdot \Lambda, \ v_{p\_short} = f_{short} \cdot \Lambda \quad (1)$$

$$v_{g\_open} = v_{p\_open} - \Lambda \cdot dv_{p\_open}/d\Lambda \quad (2)$$

$$K^2 = (v_{p\_open}^2 - v_{p\_short}^2)/v_{p\_short}^2 \quad (3)$$

$K^2$ follows similar definitions can also be calculated [45]–[47]. As this work focuses on the electrically open waveguide, we will use $v_p$ and $v_g$ throughout the paper to represent the phase and group velocities in the electrically open LiNbO$_3$.

The dispersion for Lamb waves propagating along the material X-axis and Y-axis is plotted in Fig. 4 and 5, respectively. These curves are highly dispersive. SH0 has non-zero $K^2$ along the X-axis, while S0 has non-zero $K^2$ along the Y-axis. Higher-order modes operate at higher frequencies for transducers with the same lateral dimensions and thus have higher $v_p$. $v_g$ of higher-order modes shows more complicated patterns. Unlike SH0, S0, and SAW, higher-order modes have much
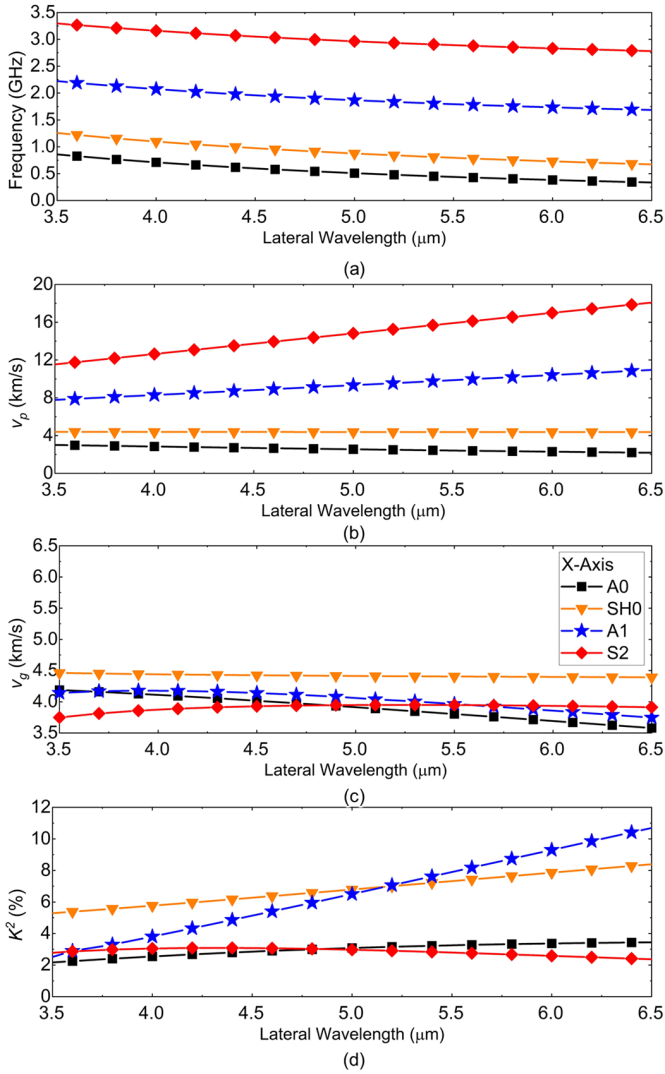
Fig. 4.   Simulated (a) frequency, (b) $v_p$, (c) $v_g$, and (d) $K^2$ of A0, SH0, A1, and S2 in 1600 nm Z-cut LiNbO$_3$ waveguide, along the material X-axis.



Fig. 5.   Simulated (a) frequency, (b) $v_p$, (c) $v_g$, and (d) $K^2$ of A0, S0, A1, and S2 in 1600 nm Z-cut LiNbO$_3$ waveguide, along the material Y-axis.

smaller $v_g$ than $v_p$, suggesting that these modes propagate at a much slower velocity. $K^2$ between 2% and 8% is extracted for various modes. $K^2$ is smaller for shorter $\Lambda$ except for S2, as only top electrodes are applied. A0, A1, and S2 show similar dispersion along X-axis and Y-axis, as $e_{15}$ equals $e_{24}$ in Z-cut LiNbO$_3$.

### C. Loss Extraction Approach and Finite Element Analysis

Frequency domain FEA is set up for showcasing the loss extraction approach (Fig. 2). 2D simulation is used for simplicity under the plane wave approximation. Perfectly matched layers (PML) are placed on the longitudinal ends of the suspended thin film, emulating the energy dissipation into the substrate. Mechanically free and electrically open boundary conditions are applied to the waveguide. A low mechanical $Q$ of the LiNbO$_3$ waveguide is set as 200 (defining imaginary loss modulus to the stiffness constants [48], [49]) for larger IL contrast in longer ADLs. Two-port S parameters are obtained from the simulation, including the IL and group delay information.
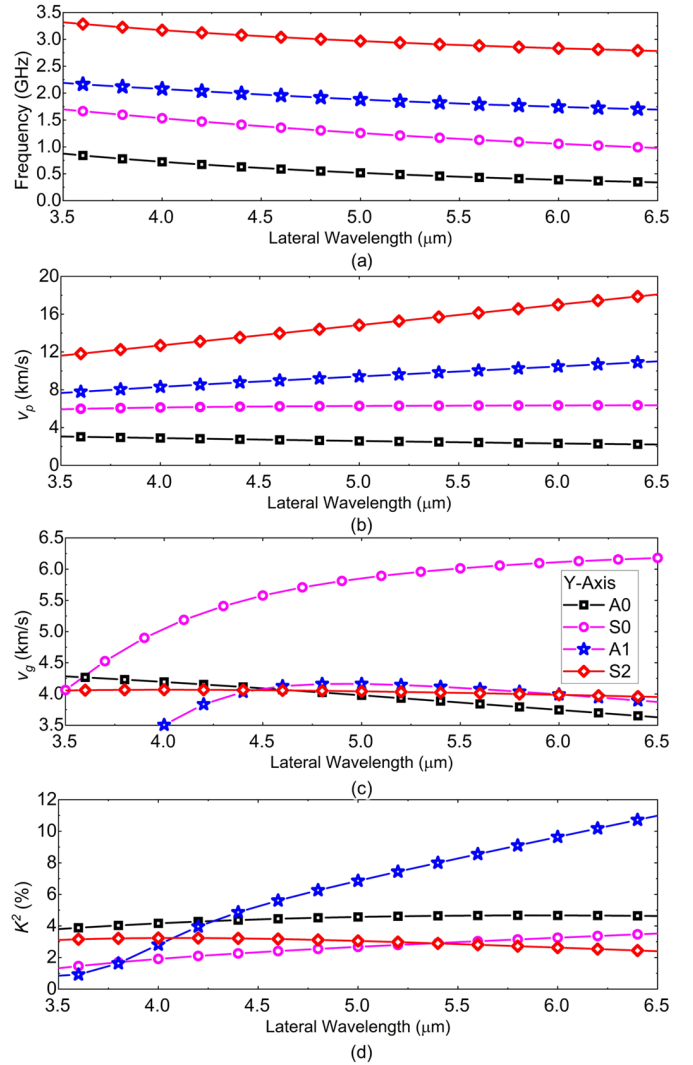
ADLs along the X-axis in Z-cut LiNbO$_3$ are first simulated. A group of ADLs with $\Lambda$ of 4.86 $\mu$m and $L_g$ between 10 and 640 $\mu$m are presented in Fig. 6 as examples, with the port impedance of 50 $\Omega$. 4 passbands are seen in the spectrum between 0 and 3.5 GHz, A0 at 0.55 GHz, SH0 at 0.87 GHz, A1 at 1.82 GHz, and S2 at 2.94 GHz [Fig. 6 (a)], matching that simulated from eigenmode FEA (Fig. 4). For short ADLs, A1 and S2 bands show lower IL, as they are better matched to the port impedance, as they are at higher frequencies. IL further increase for longer ADLs, as the wave attenuates during the propagation. Although the same acoustic $Q$ is assigned for different modes, higher-order modes show significantly faster IL increase. The reason will be explained in this subsection. The simulated group delay is shown in Fig. 6 (b). ADLs with longer $L_g$ have longer delays. Lamb modes are highly dispersive, matching the trend predicted by $v_g$ in Fig. 4 (c). PL and $v_g$ are extracted for each mode at the point with the minimum IL, and then fitted via linear regression (Fig. 7). IL and group delay are smoothed with the moving window method [50] within 60 MHz to mitigate the minor ripples due to weak resonances between the transducers [51]. The
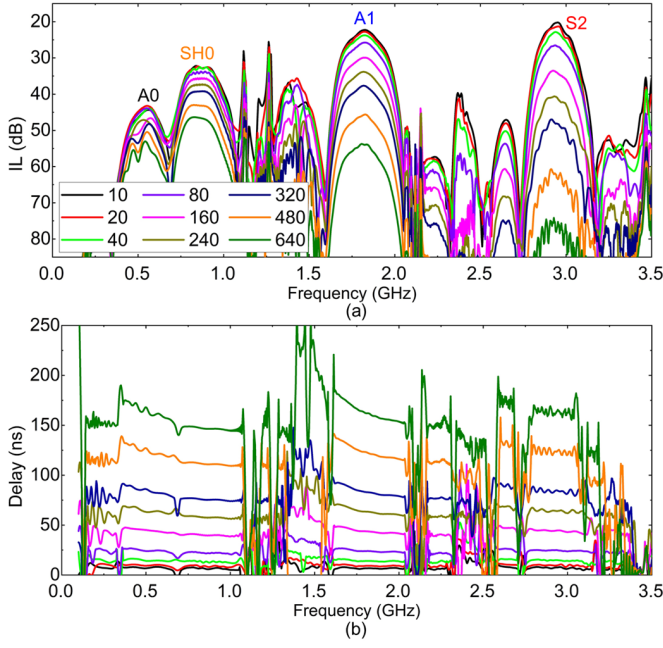
Fig. 6. Simulated (a) IL and (b) group delay of ADL with $\Lambda$ of 4.86 $\mu$m and $L_g$ between 10 and 640 $\mu$m along the X-axis in Z-cut LiNbO$_3$. A0, SH0, A1 and S2 passbands are labeled. Mechanical $Q$ of 200 is used in FEA.



Fig. 8. Simulated (a) IL and (b) group delay of ADL with $\Lambda$ of 4.86 $\mu$m and $L_g$ between 10 and 640 $\mu$m along the Y-axis in Z-cut LiNbO$_3$. A0, S0, A1 and S2 passbands are labeled. Mechanical $Q$ of 200 is used in FEA.



Fig. 7. Simulated (a) IL and (b) group delay in ADLs along the X-axis in Z-cut LiNbO$_3$. PL, $v_g$, and $Q$ of different modes are extracted for A0, SH0, A1, and S2.



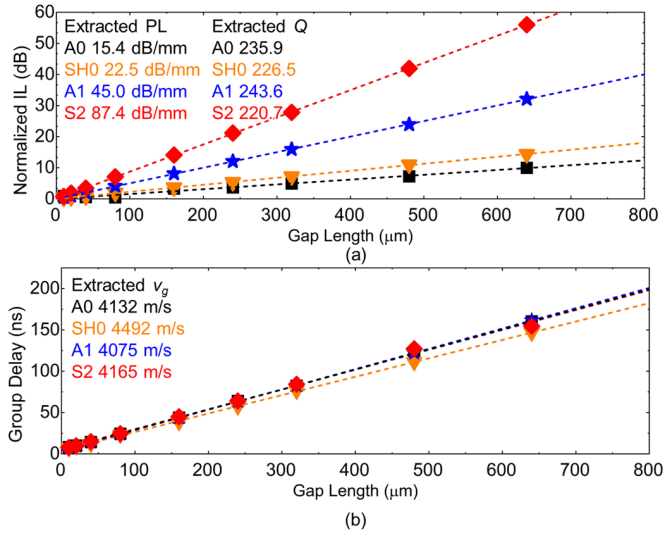Fig. 9. Simulated (a) IL and (b) group delay in ADLs along the Y-axis in Z-cut LiNbO$_3$. PL, $v_g$, and $Q$ of different modes are extracted for A0, S0, A1, and S2.

extracted PL is 15.4 dB/mm for A0, 22.5 dB/mm for SH0, 45.0 dB/mm for A1, and 87.4 dB/mm for S2, respectively. $v_g$ is 4132 m/s for A0, 4492 m/s for SH0, 4075 m/s for A1, and 4165 m/s for S2, respectively.

Note that the $Q$ extraction for higher-order modes needs special attention, as $v_p$ differs from $v_g$ in higher-order modes. $v_g$, which can be approximated as the energy velocity in weakly dissipative media [52], should be used for $Q$ extraction, instead of the phase velocity $v_p$, following the equations:

$$PL = PL_{dis} \cdot v_g/f \qquad (4)$$
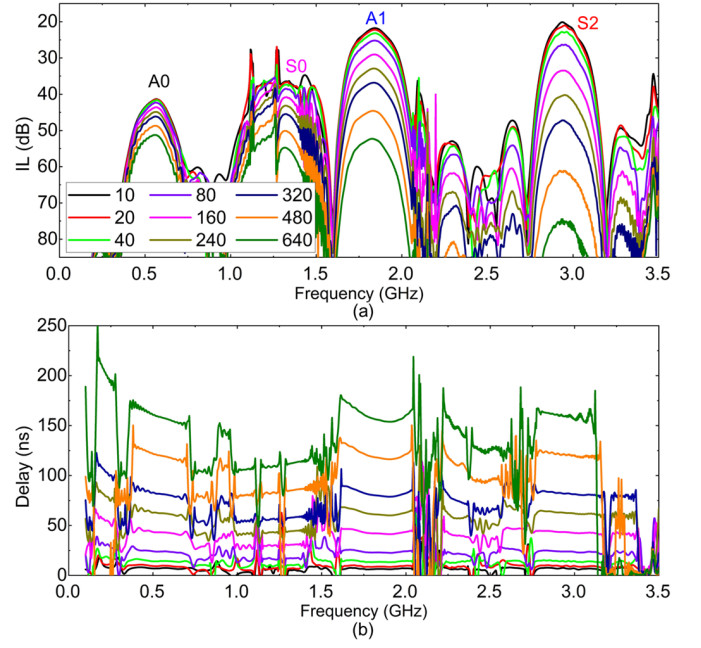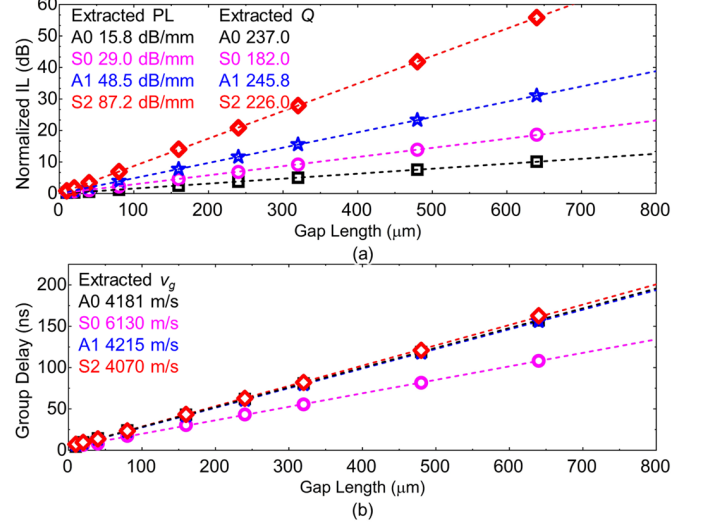
$$Q = \pi/PL \qquad (5)$$

where $PL$ is the propagation loss per cycle, with the unit of neper. $PL_{dis}$ is the propagation loss per unit distance, directly extracted from IL, with the unit of dB/mm. $v_g$ is the group velocity, with the unit of m/s. $f$ is the operating frequency, with the unit of Hz. $Q$ is the acoustic quality factor, a dimensionless quantity.

The simulated performance of ADLs along the X-axis with a set $Q$ of 200 is used to validate the process. The extracted $Q$s are 235.9 for A0, 226.5 for SH0, 243.6 for A1, 220.7 for S2, respectively, matching those predicted. The slight deviation likely originates from the smoothing and minor in-band ripples. The results verify our method of extracting attainable $Q$ using ADL testbeds instead of directly from
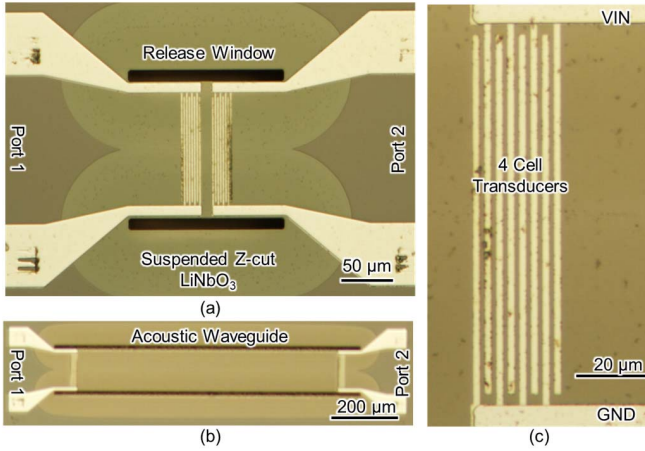
Fig. 10. Optical images of fabricated ADL testbeds in Z-cut LiNbO$_3$. (a) ADL with $\Lambda$ of 4.84 $\mu$m and $L_g$ of 10 $\mu$m. (b) ADL with $\Lambda$ of 4.84 $\mu$m and $L_g$ of 800 $\mu$m. (c) Zoomed-in transducer image.

resonators. The $Q$ standard deviations from the slope error in linear regression [53] are calculated as 13.2, 1.9, 0.6, and 0.5, respectively. The extracted $Q$s are higher than the set values, likely due to the slight reflection of the PMLs.

Similarly, ADLs along the Y-axis in Z-cut LiNbO$_3$ are simulated, showing passbands of A0 at 0.55 GHz, S0 at 1.25 GHz, A1 at 1.83 GHz, and S2 at 2.94 GHz. Strong spurious modes are seen in the S0 passband, as the non-propagating undertones of the A1 mode effectively act as one-port resonators. Following the same procedure, the extracted PL is 15.8 dB/mm for A0, 29.0 dB/mm for S0, 48.5 dB/mm for A1, and 87.2 dB/mm for S2, respectively. $v_g$ is 4181 m/s for A0, 6130 m/s for S0, 4215 m/s for A1, and 4070 m/s for S2, respectively. Using the same approach, the extracted $Q$s are 237.0 for A0, 182.0 for S0, 245.8 for A1, 226.0 for S2, also matching those predicted. The $Q$ standard deviations [53] are calculated as 1.5, 1.6, 0.2, and 0.2, respectively.

## III. FABRICATION

ADL testbeds are in-house fabricated with the process reported in [40]. The design parameters and variations are summarized in Table I, with 9 groups of ADLs with $\Lambda$ between 3.68 $\mu$m and 6.4 $\mu$m, placed along the X-axis or Y-axis in 1600 nm thick Z-cut LiNbO$_3$. Within each group, ten ADLs with the identical transducer design but different $L_g$ between 10 $\mu$m and 800 $\mu$m are implemented.

Examples of the fabricated shorter and longer ADLs are shown in Fig. 10 (a) and (b). The release windows are placed on the side for defining the acoustic waveguide while enabling the release of the structure. The transducers are placed far from the longitudinal ends of the release windows to mitigate the slight reflection from the interface. Zoomed-in view [Fig. 10 (c)] shows the 4-cell transducers designed for impedance mismatch and wideband operation.

## IV. MEASUREMENT AND DISCUSSION

### A. Attenuation of Lamb Waves in Air

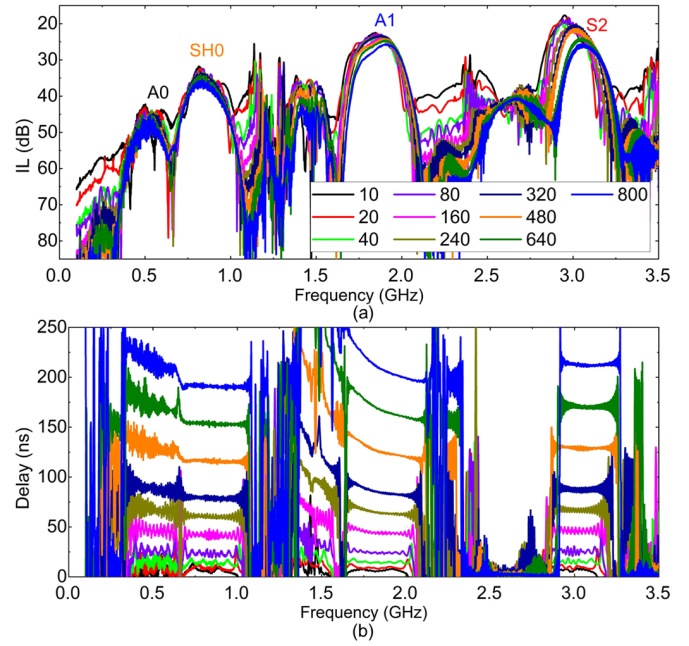The fabricated ADL testbeds are first measured at room temperature in air with a Keysight P5027A vector network



Fig. 11. Measured (a) IL and (b) group delay of ADL with $\Lambda$ of 4.86 $\mu$m and $L_g$ between 10 and 640 $\mu$m along the X-axis in Z-cut LiNbO$_3$ in air. A0, SH0, A1 and S2 passbands are labeled.

analyzer under 50 $\Omega$ port impedance. Here we first present the example ADLs to compare with the earlier simulation in Section III, before showing the summarized extracted propagation parameters and $Q$ with different wavelengths.

Measured IL and group delay of the ADL with $\Lambda$ of 4.86 $\mu$m and $L_g$ between 10 $\mu$m and 800 $\mu$m, along the X-axis in Z-cut LiNbO$_3$ are plotted in Fig. 11 (a) and (b). Like the simulation in Fig. 6, the passbands of A0, SH0, A1 and S2 are seen at 0.52 GHz, 0.84 GHz, 1.85 GHz, and 3.00 GHz, respectively. Capacitive feedthrough from the probing pads causes a slight reduction of out-of-band rejection [40]. The non-uniformity of thin-film LiNbO$_3$ (calculated around 4%) causes a shift of frequency of A1 and S2 passbands in different ADLs. A0, SH0 passbands are less affected as their frequencies are less dependent by the thickness variation. The measured group delay validates the dispersion of Lamb waves.

Following the process in Section II-C, PL and $v_g$ are extracted for Lamb waves traveling along the X-axis in 1600 nm thick LiNbO$_3$. The values are obtained at the point with minimum IL in the corresponding passband. The extracted PL [Fig. 12 (a)] is 4.78 dB/mm for A0, 3.44 dB/mm for SH0, 2.92 dB/mm for A1, and 8.06 dB/mm for S2. The extracted $v_g$ [Fig. 12 (b)] is 3835 m/s for A0, 4284 m/s for SH0, 3919 m/s for A1, and 3863 m/s for S2. Using Eqs. 4-5, the extracted $Q$s are 733.6 for A0, 1552.8 for SH0, 4401.9 for A1, and 2628.4 for S2, respectively.

Similarly, measured IL and group delay of the ADL with $\Lambda$ of 4.86 $\mu$m and $L_g$ between 10 $\mu$m and 800 $\mu$m, along the Y-axis in Z-cut LiNbO$_3$ are plotted in Fig. 13 (a) and (b). Passbands of A0, S0, A1 and S2 are seen at 0.53 GHz, 1.25 GHz, 1.87 GHz, and 3.01 GHz. The measurements match those simulated in Fig. 8. One potential issue is that amplitudes of the non-propagating A1 waves are significant compared to
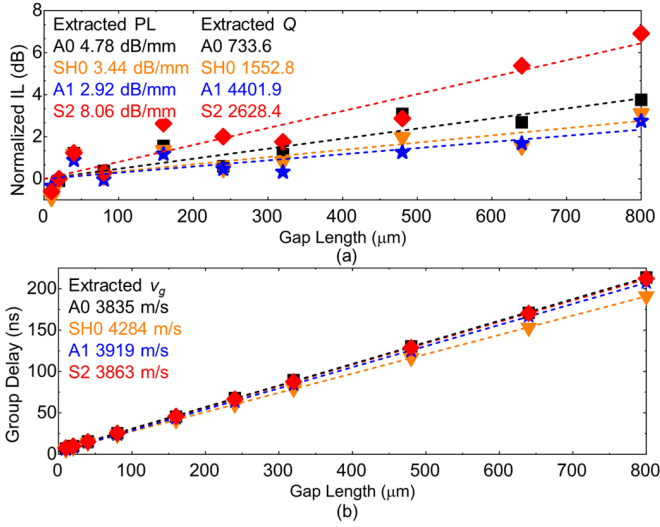
Fig. 12. Measured (a) IL and (b) group delay in ADLs along the X-axis in Z-cut LiNbO$_3$ in air. PL, $v_g$, and $Q$ are extracted for A0, SH0, A1, and S2.



Fig. 14. Measured (a) IL and (b) group delay in ADLs along the Y-axis in Z-cut LiNbO$_3$ in air. PL, $v_g$, and $Q$ are extracted for A0, S0, A1, and S2.
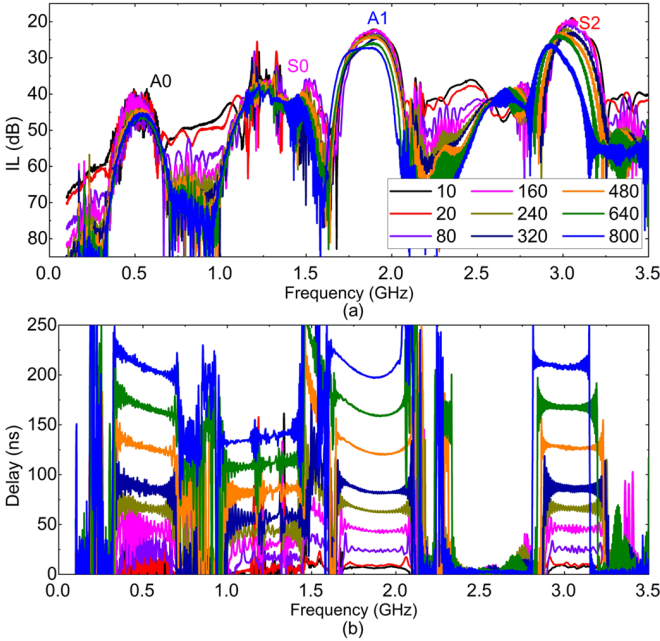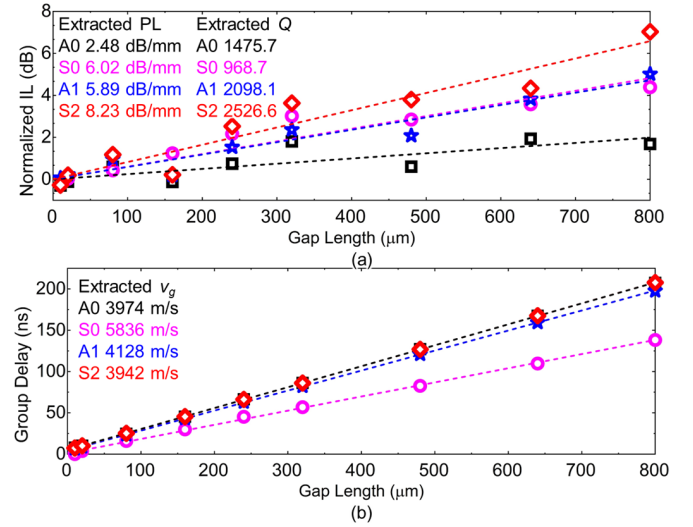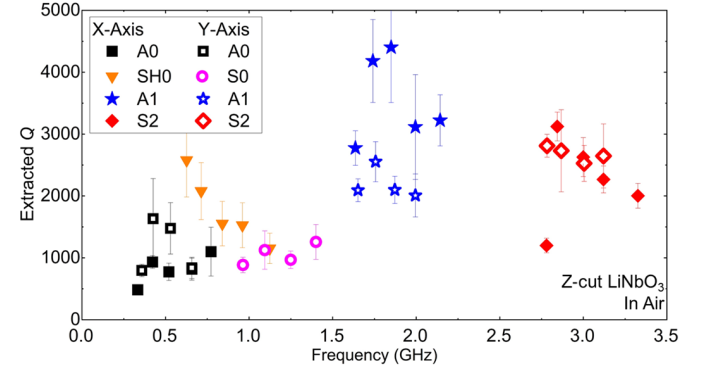


Fig. 13. Measured (a) IL and (b) group delay of ADL with $\Lambda$ of 4.86 $\mu$m and $L_g$ between 10 and 640 $\mu$m along the Y-axis in Z-cut LiNbO$_3$ in air. A0, S0, A1 and S2 passbands are labeled.



Fig. 15. Summary of extracted $Q$ and frequencies of A0, SH0, S0, A1, and S2 in Z-cut LiNbO$_3$ measured in air. Error bars from linear regression fitting are plotted.

the PL of S0 waves. Thus, the accuracy of S0 loss study is limited.

Next, PL and $v_g$ are extracted for Lamb waves traveling along the Y-axis in 1600 nm thick LiNbO$_3$. The values are obtained at the point with minimum IL in the corresponding passband. The extracted PL [Fig. 14 (a)] is 2.48 dB/mm for A0, 6.02 dB/mm for S0, 5.89 dB/mm for A1, and 8.23 dB/mm for S2. The extracted $v_g$ [Fig. 14 (b)] is 3974 m/s for A0, 5836 m/s for S0, 4128 m/s for A1, and 3942 m/s for S2. Using Eqs. 4-5, the extracted $Q$s are 1475.7 for A0, 968.7 for S0, 2098.1 for A1, and 2526.6 for S2, respectively.

ADL groups with different lateral wavelengths $\Lambda$ between 3.68 $\mu$m and 6.4 $\mu$m are studied. The extracted PL and $Q$ for different modes are summarized in Table II and Table III.

The $Q$ and operating frequencies of different Lamb modes are plotted in Fig. 15, to present a comparative study of attainable $Q$ of different Lamb waves in thin-film LiNbO$_3$. A1 and S2 modes have higher $Q$ than A0, S0, and SH0. The standard deviation of $Q$ is plotted. Further discussion will be provided in Section IV-C.

### B. Attenuation of Lamb Waves in Vacuum

ADLs are next measured with a vacuum probe station for characterizing the propagation loss of Lamb waves in vacuum at room temperature. The same devices are measured in air and vacuum, except a few damaged during the shipping between institutions. The measurement follows the same setup and extraction procedure as the previous test in air.

The PL are extracted and listed in Table IV. Similarly, the extracted $Q$s of different Lamb modes with lateral wavelengths between 3.68 $\mu$m and 6.4 $\mu$m are illustrated in Table V and Fig. 15. Taking the same group with 4.86 $\mu$m lateral wavelength as the example, along the X-axis, the extracted $Q$s are 742 for A0, 1498 for SH0, 4971 for A1, and 2651 for S2, respectively. Along the Y-axis, the extracted $Q$s are 1560 for A0, 1062 for S0, 2587 for A1, and 2710 for S2, respectively. The standard deviation of $Q$ is plotted. The deviation is higher
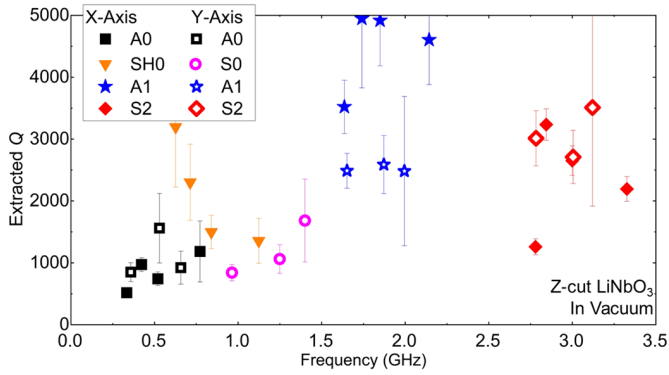
Fig. 16. Summary of extracted $Q$ and frequencies of A0, SH0, S0, A1, and S2 in Z-cut LiNbO$_3$ measured in vacuum. Error bars from linear regression fitting are plotted.

TABLE II

PL (IN AIR) OF LAMB WAVES IN Z-CUT THIN-FILM LiNbO$_3$

| $\Lambda$ (μm) | X-Axis (dB/mm) | | | | Y-Axis (dB/mm) | | | |
|---|---|---|---|---|---|---|---|---|
| | A0 | SH0 | A1 | S2 | A0 | S0 | A1 | S2 |
| 3.68 | 4.71 | 6.15 | 4.31 | 11.86 | – | – | – | – |
| 4.2 | 5.17 | 3.97 | 4.30 | 9.92 | 5.22 | 5.31 | 6.68 | 8.21 |
| 4.86 | 4.78 | 3.44 | 2.92 | 8.06 | 2.48 | 6.02 | 5.89 | 8.23 |
| 5.6 | 3.34 | 2.18 | 3.08 | 11.54 | 1.89 | 4.30 | 4.75 | 7.30 |
| 6.4 | 5.36 | 1.55 | 4.87 | 16.92 | 3.41 | 4.80 | 5.96 | 6.95 |

TABLE III

$Q$ (IN AIR) OF LAMB WAVES IN Z-CUT THIN-FILM LiNbO$_3$

| $\Lambda$ (μm) | X-Axis | | | | Y-Axis | | | |
|---|---|---|---|---|---|---|---|---|
| | A0 | SH0 | A1 | S2 | A0 | S0 | A1 | S2 |
| 3.68 | 1099 | 1153 | 3221 | 2003 | – | – | – | – |
| 4.2 | 817 | 1527 | 3114 | 2267 | 838 | 1257 | 2007 | 2646 |
| 4.86 | 774 | 1553 | 4402 | 2628 | 1476 | 969 | 2098 | 2527 |
| 5.6 | 933 | 2079 | 4182 | 3122 | 1633 | 1125 | 2554 | 2730 |
| 6.4 | 484 | 2578 | 2774 | 1199 | 796 | 885 | 2092 | 2811 |

TABLE IV

PL (IN VACUUM) OF LAMB WAVES IN Z-CUT THIN-FILM LiNbO$_3$

| $\Lambda$ (μm) | X-Axis (dB/mm) | | | | Y-Axis (dB/mm) | | | |
|---|---|---|---|---|---|---|---|---|
| | A0 | SH0 | A1 | S2 | A0 | S0 | A1 | S2 |
| 3.68 | 4.37 | 5.23 | 3.02 | 10.83 | – | – | – | – |
| 4.2 | – | – | – | – | 4.75 | 5.72 | 43.06 | 6.19 |
| 4.86 | 4.98 | 3.57 | 2.62 | 7.99 | 2.34 | 5.50 | 4.78 | 7.67 |
| 5.6 | 3.21 | 1.97 | 2.61 | 11.13 | – | – | – | – |
| 6.4 | 5.02 | 1.25 | 3.84 | 16.11 | 3.20 | 5.04 | 5.01 | 6.48 |

in vacuum, due to worse contact control in the vacuum probe station.

The extracted $Q$s in vacuum (Fig. 16) are quantitatively compared with those in air (Fig. 15). The $Q$ enhancement ratio is calculated and averaged among data from the same mode but with different lateral wavelengths. Along the X-axis, the Q enhancement factors are 3.6% for A0, 12.2% for SH0, 25.0% for A1, and 4.8% for S2. Along the Y-axis, the Q enhancement factors are 7.5% for A0, 12.9% for S0, 22.0% for A1, and 15.7% for S2. The air damping is not the dominant loss origin of GHz Lamb waves in thin-film LiNbO$_3$.

### C. Discussion

We have performed the first experimental comparison between Lamb waves of different orders in thin-film LiNbO$_3$.

TABLE V

$Q$ (IN VACUUM) OF LAMB WAVES IN Z-CUT THIN-FILM LiNbO$_3$

| $\Lambda$ (μm) | X-Axis | | | | Y-Axis | | | |
|---|---|---|---|---|---|---|---|---|
| | A0 | SH0 | A1 | S2 | A0 | S0 | A1 | S2 |
| 3.68 | 1184 | 1356 | 4604 | 2194 | – | – | – | – |
| 4.2 | – | – | – | – | 922 | 1683 | 2482 | 3510 |
| 4.86 | 742 | 1498 | 4917 | 2651 | 1560 | 1062 | 2587 | 2710 |
| 5.6 | 972 | 2302 | 4947 | 3235 | – | – | – | – |
| 6.4 | 517 | 3195 | 3520 | 1259 | 850 | 842 | 2488 | 3013 |

However, the following aspects could be improved in future works. First, we assume plane wave characteristics in the ADL waveguide. It is based on the fact that our ADL aperture is significantly longer than the lateral wavelength, and these Lamb waves have zero power flow angle (angle between the phase and group velocities [54]) along X-axis and Y-axis in Z-cut LiNbO$_3$ [40]. The minor wave diffraction and loss near the busline and release window regions might cause a slight underestimation of the acoustic $Q$. Second, the in-band ripples, originated from the bi-directional transducers, inevitably cause errors in the damping extraction of low-loss Lamb modes. ADLs with longer gap lengths (thus higher PL) are desired for higher accuracy extraction. Third, the dependency of in-plane orientations on acoustic damping is not fully investigated. Finally, a controlled study of various Lamb waves in LiNbO$_3$ stacks of different thicknesses will be of great importance.

Note that the propagation loss extracted in this work is not the ultimate performance limit for thin-film LiNbO$_3$ technology. Such $Q$s are highly dependent on the quality of the transferred thin-film LiNbO$_3$, e.g. surface roughness. The equivalent $Q$s here are at least one order of magnitude lower than those measured in bulk LiNbO$_3$ [7]. Better fabrication techniques, especially in the thin-film transfer process, could continue to advance the performance of the thin-film LiNbO$_3$ platform in the future.

### V. CONCLUSION

In this work, we experimentally extract the acoustic loss of Lamb waves in Z-cut LiNbO$_3$ thin films. ADL testbeds are designed and implemented for the comparative study of damping between modes, using a generalized approach for $Q$ extraction. The results show higher acoustic $Q$s of A1 and S2 than S0 and SH0 in air and vacuum at room temperature, advocating for further frequency scaling beyond GHz using higher-order Lamb modes. The extracted $Q$s are higher than those in resonators, pointing to improvement opportunities in the topology design and electrode optimization. The approach is readily extendable to other emerging acoustic platforms.

### REFERENCES

[1] S. Gong, R. Lu, Y. Yang, L. Gao, and A. E. Hassanien, "Microwave acoustic devices: Recent advances and outlook," *IEEE J. Microw.*, vol. 1, no. 2, pp. 601–609, Spring 2021.

[2] R. Lu and S. Gong, "RF acoustic microsystems based on suspended lithium niobate thin films: Advances and outlook," *J. Micromech. Microeng.*, Sep. 2021. [Online]. Available: https://iopscience.iop.org/article/10.1088/1361-6439/ac288f?fbclid=IwAR3GhKFhUfNu60o6Pm0wyWxxtdn1Ei7jA_071q4FVaaSMKcxnhsPNlq5-gg

[3] F. Boccardi, R. W. Heath, A. Lozano, T. L. Marzetta, and P. Popovski, "Five disruptive technology directions for 5G," *IEEE Commun. Mag.*, vol. 52, no. 2, pp. 74–80, Feb. 2014.

[4] R. Ruby, "A snapshot in time: The future in filters for cell phones," *IEEE Microw. Mag.*, vol. 16, no. 7, pp. 46–59, Aug. 2015.

[5] H. Odagawa and K. Yamanouchi, "10 GHz range extremely low-loss ladder type surface acoustic wave filter," in *Proc. IEEE Int. Ultrason. Symp.*, Jun. 1998, pp. 103–106.

[6] M. Hara *et al.*, "Super-high-frequency band filters configured with air-gap-type thin-film bulk acoustic resonators," *Jpn. J. Appl. Phys.*, vol. 49, no. 7, Jul. 2010, Art. no. 07HD13.

[7] I. L. Bajak, A. McNab, J. Richter, and C. D. W. Wilkinson, "Attenuation of acoustic waves in lithium niobate," *J. Acoust. Soc. Amer.*, vol. 69, no. 3, pp. 689–695, Mar. 1981.

[8] R. T. Schermer and T. H. Stievater, "Millimeter-wave dielectric properties of highly refractive single crystals characterized by waveguide cavity resonance," *IEEE Trans. Microw. Theory Techn.*, vol. 67, no. 3, pp. 1078–1087, Mar. 2019.

[9] R. Lu, Y. Yang, and S. Gong, "Acoustic loss in thin-film lithium niobate: An experimental study," *J. Microelectromech. Syst.*, vol. 30, no. 4, pp. 632–641, Aug. 2021.

[10] Y. Yang, R. Lu, L. Gao, and S. Gong, "10–60-GHz electromechanical resonators using thin-film lithium niobate," *IEEE Trans. Microw. Theory Techn.*, vol. 68, no. 12, pp. 5211–5220, Dec. 2020.

[11] K. Matsumoto, M. Kadota, and S. Tanaka, "High frequency thickness expansion mode bulk acoustic wave resonator using LN single crystal thin plate," *Jpn. J. Appl. Phys.*, vol. 59, no. 3, p. 36506, 2020.

[12] M. Kadota, T. Ogami, K. Yamamoto, H. Tochishita, and Y. Negoro, "High-frequency Lamb wave device composed of MEMS structure using LiNbO$_3$ thin film and air gap," *IEEE Trans. Ultrason., Ferroelect., Freq. Control*, vol. 57, no. 11, pp. 2564–2571, Nov. 2010.

[13] T. Kimura, M. Omura, Y. Kishimoto, and K. Hashimoto, "Comparative study of acoustic wave devices using thin piezoelectric plates in the 3–5-GHz range," *IEEE Trans. Microw. Theory Techn.*, vol. 67, no. 3, pp. 915–921, Mar. 2019.

[14] M. Bousquet *et al.*, "Single-mode high frequency LiNbO$_3$ film bulk acoustic resonator," in *Proc. IEEE Int. Ultrason. Symp. (IUS)*, Oct. 2019, pp. 84–87.

[15] V. Plessky, S. Yandrapalli, P. J. Turner, L. G. Villanueva, J. Koskela, and R. B. Hammond, "5 GHz laterally-excited bulk-wave resonators (XBARs) based on thin platelets of lithium niobate," *Electron. Lett.*, vol. 55, no. 2, pp. 98–100, Nov. 2018.

[16] C. Cassella, G. Chen, Z. Qian, G. Hummel, and M. Rinaldi, "RF passive components based on aluminum nitride cross-sectional Lamé-mode MEMS resonators," *IEEE Trans. Electron Devices*, vol. 64, no. 1, pp. 237–243, Jan. 2017.

[17] M. Assylbekova, G. Chen, M. Pirro, G. Michetti, and M. Rinaldi, "Aluminum nitride combined overtone resonator for millimeter wave 5G applications," in *Proc. MEMS*, Jan. 2021, pp. 202–205.

[18] M. Assylbekova, G. Chen, G. Michetti, M. Pirro, L. Colombo, and M. Rinaldi, "11 GHz lateral-field-excited aluminum nitride cross-sectional Lamé mode resonator," in *Proc. Joint Conf. IEEE Int. Freq. Control Symp.*, Jul. 2020, pp. 1–4.

[19] G. Chen and M. Rinaldi, "AlN combined overtone resonators for the 5G mmWave spectrum," 2019, *arXiv:1912.04515*. [Online]. Available: http://arxiv.org/abs/1912.04515

[20] M. Park, J. Wang, and A. Ansari, "High-overtone thin film ferroelectric AlScN-on-silicon composite resonators," *IEEE Electron Device Lett.*, vol. 42, no. 6, pp. 911–914, Jun. 2021.

[21] J. Wang, M. Park, S. Mertin, T. Pensala, F. Ayazi, and A. Ansari, "A film bulk acoustic resonator based on ferroelectric aluminum scandium nitride films," *J. Microelectromech. Syst.*, vol. 29, no. 5, pp. 741–747, Oct. 2020.

[22] C. Moe *et al.*, "Highly doped AlScN 3.5 GHz XBAW resonators with 16% k2eff for 5G RF filter applications," in *Proc. IEEE Int. Ultrason. Symp. (IUS)*, Sep. 2020, pp. 1–4.

[23] R. Vetury, M. D. Hodge, and J. B. Shealy, "High power, wideband single crystal XBAW technology for sub-6 GHz micro RF filter applications," in *Proc. IEEE Int. Ultrason. Symp. (IUS)*, Oct. 2018, pp. 206–212.

[24] R. Wang, S. A. Bhave, and K. Bhattacharjee, "Design and fabrication of S$_0$ Lamb-wave thin-film lithium niobate micromechanical resonators," *J. Microelectromech. Syst.*, vol. 24, no. 2, pp. 300–308, Apr. 2015.

[25] S. Gong and G. Piazza, "Design and analysis of lithium-niobate-based high electromechanical coupling RF-MEMS resonators for wideband filtering," *IEEE Trans. Microw. Theory Techn.*, vol. 61, no. 1, pp. 403–414, Dec. 2013.

[26] M. Faizan and L. G. Villanueva, "Frequency-scalable fabrication process flow for lithium niobate based Lamb wave resonators," *J. Micromech. Microeng.*, vol. 30, no. 1, p. 15008, 2019.

[27] L. Colombo, A. Kochhar, G. Vidal-Álvarez, and G. Piazza, "X-cut lithium niobate laterally vibrating MEMS resonator with figure of merit of 1560," *J. Microelectromech. Syst.*, vol. 27 no. 4, pp. 602–604, Aug. 2018.

[28] R. H. Olsson, "A high electromechanical coupling coefficient SH0 Lamb wave lithium niobate micromechanical resonator and a method for fabrication," *Sens. Actuators A, Phys.*, vol. 209, pp. 183–190, Mar. 2014.

[29] S. Tanaka and M. Kadota, "IDT-based acoustic wave devices using ultrathin lithium niobate and lithium tantalate," in *Proc. IEEE Int. Freq. Control Symp.*, Jul. 2020, pp. 1–3.

[30] M. Faizan and L. G. Villanueva, "Optimization of inactive regions of lithium Niobate shear mode resonator for quality factor enhancement," *J. Microelectromech. Syst.*, vol. 4, pp. 1–6, Mar. 2021.

[31] A. Kochhar, A. Mahmoud, Y. Shen, N. Turumella, and G. Piazza, "X-cut lithium niobate-based shear horizontal resonators for radio frequency applications," *J. Microelectromech. Syst.*, vol. 29, no. 6, pp. 1464–1472, Dec. 2020.

[32] R. Lu, Y. Yang, S. Link, and S. Gong, "A1 resonators in 128° Y-cut lithium niobate with electromechanical coupling of 46.4%," *J. Microelectromech. Syst.*, vol. 29, no. 3, pp. 313–319, Jun. 2020.

[33] W. D. Braun *et al.*, "Optimized resonators for piezoelectric power conversion," *IEEE Open J. Power Electron.*, vol. 2, pp. 212–224, 2021.

[34] R. Lu, Y. Yang, S. Link, and S. Gong, "Enabling higher order Lamb wave acoustic devices with complementarily oriented piezoelectric thin films," *J. Microelectromech. Syst.*, vol. 29, no. 5, pp. 1332–1346, Oct. 2020.

[35] R. Lu and S. Gong, "A 15.8 GHz A6 mode resonator with Q of 720 in complementarily oriented piezoelectric lithium niobate thin films," in *Proc. IFCS*, Jun. 2021.

[36] B. A. Auld, *Acoustic Fields and Waves in Solids*. Baltimore, MD, USA: Krieger, 1990.

[37] J. Segovia-fernandez *et al.*, "Anchor losses in AlN contour mode resonators," *J. Microelectromech. Syst.*, vol. 24, no. 2, pp. 1–11, Apr. 2014.

[38] B. Kim *et al.*, "Temperature dependence of quality factor in MEMS resonators," *J. Microelectromech. Syst.*, vol. 17, no. 3, pp. 755–766, 2008.

[39] S. Ghaffari *et al.*, "Accurate modeling of quality factor behavior of complex silicon MEMS resonators," *J. Microelectromech. Syst.*, vol. 24, no. 2, pp. 276–288, Apr. 2015.

[40] R. Lu, Y. Yang, M.-H. Li, M. Breen, and S. Gong, "5-GHz antisymmetric mode acoustic delay lines in lithium niobate thin film," *IEEE Trans. Microw. Theory Techn.*, vol. 68, no. 2, pp. 573–589, Feb. 2020.

[41] R. Lu, Y. Yang, S. Link, and S. Gong, "Low-loss 5-GHz first-order antisymmetric mode acoustic delay lines in thin-film lithium niobate," *IEEE Trans. Microw. Theory Techn.*, vol. 69, no. 1, pp. 541–550, Jan. 2021.

[42] C. S. Hartmann and B. P. Abbott, "Overview of design challenges for single phase unidirectional SAW filters," in *Proc. IEEE Int. Ultrason. Symp.*, Dec. 1989, pp. 79–89.

[43] D. M. Pozar, *Microwave Engineering*. Hoboken, NJ, USA: Wiley, 2009.

[44] *IEEE Standard on Piezoelectricity*, Standard 176-1987, 1988. [Online]. Available: https://ieeexplore.ieee.org/document/26560

[45] E. L. Adler, "Electromechanical coupling to Lamb and shear-horizontal modes in piezoelectric plates," *IEEE Trans. Ultrason., Ferroelectr., Freq. Control*, vol. 36, no. 2, pp. 223–230, Mar. 1989.

[46] K. Hashimoto, *Surface Acoustic Wave Devices in Telecommunications: Modelling and Simulation*. Berlin, Germany: Springer-Verlag, 2000. [Online]. Available: https://www.springer.com/gp/book/9783540672326

[47] D. Royer and E. Dieulesaint, *Elastic waves in solids: Free and Guided Propagation*, vol. 1. Berlin, Germany: Springer, 1996.

[48] A. K. Chopra, *Dynamics of Structures*. London, U.K.: Pearson, 2007.

[49] *Structural Mechanics Module User's Guide*, ComsoL, Comsol AB, Stockholm, 2012.

[50] J. S. Simonoff, *Smoothing Methods in Statistics*. New York, NY, USA: Springer-Verlag, 1996. [Online]. Available: https://www.springer.com/gp/book/9780387947167

[51] R. Lu, T. Manzaneque, Y. Yang, M.-H. Li, and S. Gong, "Gigahertz low-loss and wideband S0 mode lithium niobate acoustic delay lines," *IEEE Trans. Ultrason., Ferroelectr., Freq. Control*, vol. 66, no. 8, pp. 1373–1386, Aug. 2019.

[52] A. Bers, "Note on group velocity and energy propagation," *Amer. J. Phys.*, vol. 68, no. 5, pp. 482–484, May 2000.

[53] A. C. Rencher and G. B. Schaalje, *Linear Models in Statistics*. Hoboken, NJ, USA: Wiley, 2008.

[54] I. E. Kuznetsova, B. D. Zaitsev, A. A. Teplykh, S. G. Joshi, and A. S. Kuznetsova, "The power flow angle of acoustic waves in thin piezoelectric plates," *IEEE Trans. Ultrason., Ferroelectr., Freq. Control*, vol. 55, no. 9, pp. 1984–1991, Sep. 2008.

**Ruochen Lu** (Member, IEEE) received the B.E. degree (Hons.) in microelectronics from Tsinghua University, Beijing, China, in 2014, and the M.S. and Ph.D. degrees in electrical engineering from the University of Illinois at Urbana–Champaign (UIUC), Urbana, IL, USA, in 2017 and 2019, respectively. He is currently an Assistant Professor with the Department of Electrical and Computer Engineering, The University of Texas at Austin. His research primarily focuses on developing chip-scale acoustic and electromagnetic components and microsystems for RF applications. His works aim to demonstrate reconfigurable and tunable RF functions using novel MEMS platforms, toward higher operating frequencies and more efficient transduction between the EM and acoustic domains. In addition, he works on ultrasonic transducers and multi-physics hybrid microsystems for signal processing, sensing, and computing applications. He received the Best Student Paper Awards at the 2017 IEEE International Frequency Control Symposium and 2018 IEEE International Ultrasonics Symposium.
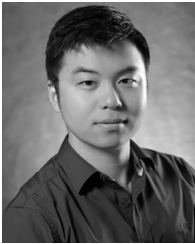
**Yansong Yang** (Member, IEEE) received the B.S. degree in electrical and electronic engineering from Huazhong University of Science and Technology, Wuhan, China, in 2014, and the M.S. and Ph.D. degrees in electrical engineering from the University of Illinois at Urbana–Champaign, Urbana, IL, USA, in 2017 and 2019, respectively. He is currently a Post-Doctoral Researcher with the University of Illinois at Urbana–Champaign. He will be joining The Hong Kong University of Science and Technology as an Assistant Professor of electronics and computer engineering in January 2022. His research interests include design and microfabrication techniques of RF MEMS resonators, filters, switches, and photonic integrated circuits. He has won the 2nd Place in the Best Paper Competition at the 2018 IEEE International Microwave Symposium, and the

best Paper Award at 2019 IEEE International Ultrasonics Symposium. He was also the Finalist of the Best Paper Award at 2018 IEEE International Frequency Control Symposium and the Advanced Practices Paper Competition Award at 2020 IEEE International Microwave Symposium. He was also a recipient of the 2019 P. D. Coleman Graduate Research Award from the Department of Electrical and Computer Engineering at UIUC.

**Songbin Gong** (Senior Member, IEEE) received the Ph.D. degree in electrical engineering from the University of Virginia, Charlottesville, VA, USA, in 2010. He is currently an Associate Professor and an Intel Alumni Fellow with the Department of Electrical and Computer Engineering and the Micro and Nanotechnology Laboratory, University of Illinois at Urbana–Champaign, Urbana, IL, USA. His research primarily focuses on design and implementation of radio frequency microsystems, components, and subsystems for reconfigurable RF front ends. In addition, his research explores hybrid microsystems based on the integration of MEMS devices with photonics or circuits for signal processing and sensing. He is a Technical Committee Member of the IEEE International Microwave Symposium, International Frequency Control Symposium, and International Ultrasonic Symposium. He was a recipient of the 2014 Defense Advanced Research Projects Agency Young Faculty Award, the 2017 NASA Early Career Faculty Award, the 2019 UIUC College of Engineer Dean's Award for Excellence in Research, and the 2019 Ultrasonics Early Career Investigator Award. Along with his students and postdoctoral scholars, he received the Best Paper Awards from the 2017 and 2019 IEEE International Frequency Control Symposium, the 2018, 2019, and 2020 International Ultrasonics Symposium, and won the 2nd and 3rd place in Best Paper Competition at the 2018 and 2020 IEEE International Microwave Symposium. He serves as the Chair for MTT TC6 and an Associate Editor for IEEE TRANSACTIONS ON ULTRASONICS, FERROELECTRICS, AND FREQUENCY CONTROL, IEEE JOURNAL OF MICROELECTROMECHANICAL SYSTEMS, and IEEE JOURNAL OF MICROWAVES.